

PARAMETER DETERMINATION AND EXPERIMENTAL VALIDATION OF A WIRE FEED ADDITIVE MANUFACTURING MODEL

Kannan Suresh Kumar*, Todd E. Sparks* and Frank Liou*

* Department of Mechanical and Aerospace Engineering, Missouri University of Science and Technology, Rolla MO, 65409

REVIEWED

ABSTRACT

Laser metal deposition with wire feed is one of the additive manufacturing methods with great scope and robustness. Process parameters plays an important role in controlling the process and obtaining an ideal manufactured part. Simulations tools are highly essential in determining the ideal parameters and melt pool conditions. The current work is a transient 3D model of wire feed additive manufacturing which realizes the heat transfer and fluid flow behavior of the process with varying laser power and power density. The model was programmed in Python and a 1 KW Gaussian beam fiber laser was used to conduct experiments. The effect of laser exposure to the scanned and deposited profile on Ti-6Al-4V alloy is obtained. The comparison of simulation and experimental results shows that this model can successfully predict the temperature profile, and solidified metal profile. The optimum input parameters based on material properties can be identified using the model.

1 INTRODUCTION

Additive manufacturing is a highly promising manufacturing method which has a wide range of applications in the aerospace, automobile and rapid prototyping industries. Additive manufacturing process is a successful alternative to the traditional subtractive manufacturing processes like machining. Manufacturing parts with complex geometries is the greatest challenge in the manufacturing industry which can be accomplished with additive manufacturing methodologies. The layer by layer addition of materials to form a complete part with the help of a heat source like laser or electron beam is called Directed Energy Deposition (DED). The high energy heat source forms a melt pool into which powder or wire is injected, therefore continuously building the part [1]. Directed Energy Deposition (DED) covers a range of terminology: 'Laser engineered net shaping (LENS), directed light fabrication, direct metal deposition (DMD), 3D laser cladding' etc.

Wire fed additive manufacturing is a highly promising additive manufacturing methodology in which a metal wire is used as the additive material and laser or electron beam as the power source. Deposition using wire and electron beam as the power source is shown in Figure 1.1 [NASA EBF3]. The wire feed additive manufacturing process involves a low velocity scan speed at higher power where the wire is directed into the integration region between the laser and the substrate [2]. The major challenges in wire fed additive manufacturing to deposit an ideal part are geometry related process parameters like substrate geometry, substrate dimensions,

wire geometry, wire diameter, angle of feed and wire feed rate which must be carefully controlled to achieve the required part geometry and surface finish. A comprehensive review of the wire feed additive manufacturing process can be found in the reference [1].



Figure 1.1: Wire feed additive manufacturing

An ideal wire feed additive manufacturing systems consists of a high power laser, wire feed system, shielding gas input and a substrate to which the material is deposited. The schematic diagram of wire fed additive manufacturing is illustrated in Figure 1.2. The wire feed system controls the critical parameters like wire feed rate, direction and angle of feed which determines the orientation of each layer and affects the required part dimensions and surface finish. The high power laser generates a melt pool on the substrate material, to which the wire is fed continuously to form layer by layer deposits. Most often the laser system and wire feed system will be linked to one head which makes the laser scan speed and wire feed rates critical parameter of the process

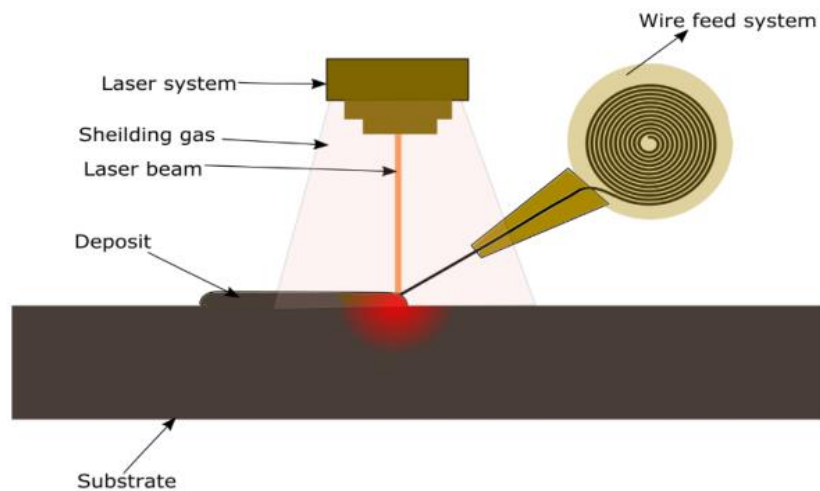


Figure 1.2: Schematic diagram of wire feed additive manufacturing system

The process under study involves highly complex thermo-mechanical and thermo-fluid phenomena like heat transfer, phase changes and solidification. The phase changes involve fluid properties of the molten metal like surface tension, viscosity and thermal expansion. The geometrical parameters, material parameters, combined with thermal and fluid characteristics makes the process highly complex which makes it challenging to experimentally determine the ideal conditions for wire deposition process. Hence a highly efficient numerical model which can effectively predict the thermal and fluid changes in the process is developed which is the objective of the current work.

1.1 Literature Review

Significant previous attempts have been made in numerical modeling of additive manufacturing process to establish the relationships between process parameters and efficiently predict the deposition process. Tang et al. [3] developed a transient model to predict the heat transfer and fluid flow of the melt pool during the EBF3 process of Ti-6Al-4V alloy. The fluid flow of the melt pool in this approach is driven by recoil pressure of vapor, impacting force of the droplet, thermal capillarity force and surface tension. In this model only a droplet mode of the wire dripping to the substrate is considered for computational efficiency. However the geometry of the molten metal is assumed to be spherical and molten fluid is assumed to be at a constant temperature in this study. Fan and Liou [4] have made significant approach in modeling laser based power feed additive manufacturing using VOF (volume of fluid) method. This method is based on Navier-Stokes fluid calculations to simulate the free surface flow and requires significant computation time. An FEA model was developed by Krol et al. [5] to study the residual stresses developing in the additive manufacturing process by neutron diffraction. This paper focuses on adjusting support structure orientation to reduce residual stresses in the additive manufacturing process. Nie et al [6] developed an FEA model of microstructure evolution of Nb bearing nickel based super alloy. The model was developed by combining FEM methods and stochastic analysis and the primary concentration of the study was nucleation and dendrite growth during solidification rather than on deposition.

Modeling of powder feed additive manufacturing process using an FEA model by the efforts of Heigel et al. [7] primarily focuses on the convection. This paper pointed out that convection is an important factor in the simulation since it affects the residual stress, microstructure and material properties. However no significant numerical implementation have been made in the fluid part of the model. An FEA model was developed by Michaleris [8] to study the effects of convection and radiation in the numerical modeling of layer by layer additive manufacturing process using quiet and inactive element method. This study primarily focuses on the temperature effects of the process and its variation with respect to the parameters with very limited approach in the fluid modeling and solidification. The model developed by Fox and Beuth [9] predicts the melt pool depth and width using an FEA approach. This model however ignores the measurement of contact angle and deposit heights which are parameters to be measured to establish a strong model to experiment validation. Shen and Chou [10] developed an FE model to establish the preheating effects in electron beam additive manufacturing of Ti-6Al-4V alloy. This approach lacks the experimental validation and the accuracy of the model needs to be measured. Similar attempts of multi-phase modeling have been achieved in laser welding

process. Pang et al. [11] [12] simulated deep penetration laser welding considering complex fluid phenomenon. Similar attempts have been made by Casalino et al [13] and Franco et al. [14] using FEA modeling approaches.

The objective of the current work is to model the wire feed additive manufacturing process taking into consideration the effects of heat transfer and fluid flow of the molten metal during the process. The motivation of this approach is the poor computational efficiency of the previous modeling approaches to efficiently simulate a complete single layer deposit by considering the effects of fluid characteristics of the material and its effects on critical measurable outcomes in the process.

2 MATHEMATICAL MODELING

2.1 Assumptions

2.1.1 Laser Beam. In the current model the laser is assumed to have a Gaussian beam profile. The distribution of laser power intensities in a Gaussian beam is shown in Figure 2.1 [15]. The numerical solution to the Gaussian beam profile was evaluated from the equation written as:

$$P(r) = P_0 e^{\left(\frac{-2r^2}{r_0^2}\right)} \quad (1)$$

where P is the calculated power at radius r, P_0 the given laser power, r_0 the radius of the laser beam and r the current radius.

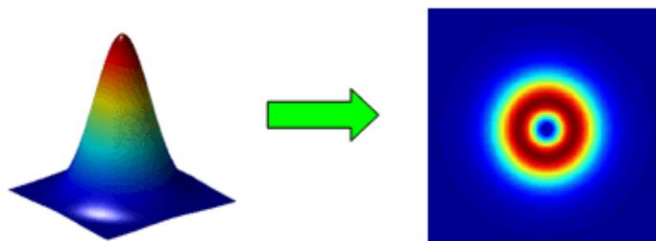


Figure 2.1: Gaussian laser beam profile

2.1.2 Ray Traced Laser. The laser beam in the current model is developed and projected on to the substrate using a more realistic “ray-traced laser”. With the ray-traced laser, the heat source is applied to the first object on the path of the laser beam. This projected laser will cast a

shadow of the solid that obstructs the rays in the substrate, which is more realistic than applying laser power onto the substrate alone. This approach is better explained in the Figure 2.2, which shows the laser projected onto a substrate with a solid in between, with and without ray-tracing.

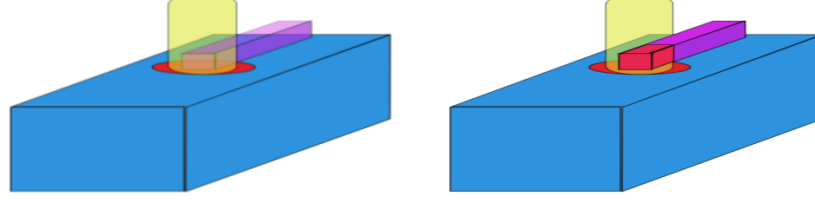


Figure 2.2: Schematic diagram of laser beam without and with ray tracing

The ray traced laser approach significantly reduces the numerical complexity of identifying objects in the simulation domain and hence enhances the flexibility of the model to accept any orientation, shape and speed of the wire and the substrate. This laser implementation provides a more realistic heat and fluid model which is critical in the wire feed additive manufacturing.

2.2 Heat Model

The heat model implemented in the current approach obeys the general laws and its direct application. The heat transfer by conduction obeys Fourier's law which states that the rate of heat conduction q is proportional to the heat transfer area (A) and the temperature gradient $\frac{\partial T}{\partial x}$.

$$q_{conduction} = -kA \frac{\partial T}{\partial x} \quad (2)$$

where k is the thermal conductivity, with unit $W/m \cdot K$. The model is assumed to be planar layers in 3 dimensions [16]. The 3 dimensional heat conduction equation in Cartesian coordinates implemented in the current model is written as:

$$\rho c_p \frac{\partial T}{\partial t} = k \left(\frac{\partial^2 T}{\partial x^2} + \frac{\partial^2 T}{\partial y^2} + \frac{\partial^2 T}{\partial z^2} \right) \quad (3)$$

where ρ is the density, c_p the specific heat. The current model is considering convection from the surfaces of parts exposed to the outside medium [17]. The rate of heat exchange between air of temperature T_a and a face of a solid of area A at temperature T_s obeys the Newton's law of cooling which can be written as:

$$q_{convection} = hA(T_s - T_a) \quad (4)$$

where the term h is the convection heat transfer coefficient. The surrounding medium is assumed to be air with convection heat transfer coefficient (h) $10 W/(m^2 K)$. In the current model only natural convection is taken into consideration. The motion of the fluid adjacent to a

solid face is caused by forces induced by changes in the density of the fluid due to differences in temperature between the solid and the surrounding air.

The radiation losses are calculated from Stefan – Boltzman Law [18]. Stefan-Boltzmann law states that the total emissive power of a blackbody, E_b , is given by:

$$E_b = \sigma T^4 \quad (5)$$

where σ is the Stefan-Boltzmann constant $5.67 \times 10^{-8} \text{ W}/(\text{m}^2 \text{K}^4)$ and T is the absolute temperature of the blackbody. When a body of a surface area (A) is immersed in a medium with ambient temperature T_a , the net rate of heat radiated by the body is given by:

$$q_{\text{radiation}} = \sigma A(T_s^4 - T_a^4) \quad (6)$$

where T_s is the absolute temperature of the solid, T_a absolute temperature of the surrounding medium (in the current model surrounding medium is air with ambient temperature 298 K). The model also realizes the heat absorbed or released during the phase change process given by equation (7) where m is the mass of the element, L_f is the latent heat fusion of Ti-64 (Table 2.1) and q is the energy released or absorbed during phase change.

$$q_{\text{latent heat}} = m \cdot L_f \quad (7)$$

2.2.1 Boundary Conditions. The energy balance at the free surface takes into consideration laser irradiation, convective losses, and radiative losses given by the following boundary equation [4]:

$$k \frac{\partial T}{\partial n} = \frac{\eta P_{\text{laser}}}{\pi R^2} - h(T_s - T_a) - \varepsilon \sigma (T_s^4 - T_a^4) \quad (8)$$

where η is the laser absorption coefficient, P_{laser} is the power of the laser obtained from equation (1), R is the radius of the laser spot, n is the normal vector at the local interface, and ε is the emissivity. The above boundary condition applies to the top surface of the substrate based on the previously mentioned ray tracing methodology. The radiative losses are negligible in the side and bottom surfaces. The sides and bottom boundary condition equation considered in this study is as follows [4]:

$$K \frac{\partial T}{\partial n} + h(T_s - T_a) = 0 \quad (9)$$

The heat model is implemented by a general finite difference algorithm which will switch to a finite volume fluid model upon melting. The material properties considered in this model are listed below in Table 2.1.

Table 2.1 : Material properties of Ti-6Al-4V considered in the model

Properties	Value	References
Liquidus Temperature (K)	1923.0	[19]
Solidus Temperature (K)	1877.0	[20]
Solid specific heat (Cp) $J Kg^{-1}K^{-1}$	$\begin{cases} 483.04 + 0.215T & T \leq 1268 \\ 412.7 + 0.1801T & 1268 < T < 1923 \end{cases}$	[19]
Liquid specific heat (Cp) $J Kg^{-1}K^{-1}$	831	[19]
Thermal conductivity (K) $Wm^{-1}K^{-1}$	$\begin{cases} 1.2595 + 0.0157T & T \leq 1268K \\ 3.5127 + 0.0127T & 1268 < T \leq 1923 \end{cases}$	[19]
Solid density ($Kg m^{-3}$)	$4420 - 0.154 (T - 298)$, T in K	[19]
Liquid density ($Kg m^{-3}$)	$3920 - 0.68 (T - 1923)$, T in K	[19]
Latent heat of fusion ($J Kg^{-1}$)	2.86×10^5	[19]
Dynamic viscosity (μ) $(Nm^{-1}s^{-1})$	3.25×10^{-3} (1923K), 3.03×10^{-3} (1973K) 2.66×10^{-3} (2073K), 2.36×10^{-3} (2173K)	[19]
Radiation emissivity (ϵ)	$0.1536 + 1.8377 \times 10^{-4} (T - 300K)$	[21]
Surface tension coefficient (γ) (Nm^{-1})	$1.525 - 0.28 \times 10^{-3} (T - 1941K)$	[19]
Thermal expansion coefficient (α) (K^{-1})	1.1×10^{-5}	[19]
Laser absorption coefficient (η)	0.4	[4]
Ambient temperature (K)	298	[4]
Convection coefficient (h) (Wm^2K^{-1})	10	[4]

2.3 Fluid Model

The fluid in the current work is considered to be Smoothed Particle Hydrodynamics (SPH) particles. SPH is a position based dynamics approach which is computationally efficient in solving fluid problems. The primary advantage of SPH over other computation techniques is that it is a mesh-free Lagrangian method. The SPH method works by dividing the fluid into a set of discrete elements, referred to as a “particles” which have a spatial distance (known as the "smoothing length" and typically represented in equations by h) over which their properties are

"smoothed" by a kernel function [22]. This means that the physical quantity of any particle can be obtained by summing the relevant properties of all the particles that lie within the range of the kernel. According to SPH the equation of any quantity A, at a distance r is given by the equation [22]:

$$A(r) = \sum_j m_j \frac{A_j}{\rho_j} W(|r - r_j|, h) \quad (10)$$

where terms m_j is the mass of particle j, ρ_j the density of particle j, A_j the quantity under consideration of particle j, W the kernel function and h is the smoothing length also called as support radius. A pictorial representation of the 2 kernel functions are shown in Figure 2.5 [23] [24].

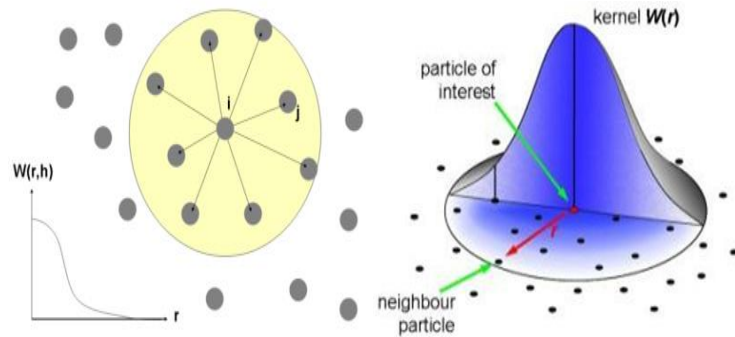


Figure 2.3: Pictorial representation of cubic spline kernel function

2.3.1 Surface Tension. The surface tension model can be evaluated by the above mentioned SPH methodology by considering fluid to fluid forces called cohesion and fluid to solid forces called adhesion. The current method uses a single surface tension function to evaluate the cohesion and adhesion effects which was proposed by Akinci et al. [25] which can be written mathematically as:

$$F_{i \leftarrow j}^{Surface\ Tension} = -\gamma m_i m_j W(|X_i - X_j|, h) \frac{X_i - X_j}{|X_i - X_j|} \quad (11)$$

where i and j denotes the neighboring particles, m is the mass of the particle, γ the surface tension coefficient revealed in Table 2.1 and W is the kernel function which can be written as:

$$W(r) = \frac{32}{\pi h^9} \begin{cases} 0 & r \geq 0.95 \times L \wedge r \leq 1.05 \times L \\ (h-r)^3 r^3 & r > \frac{h}{2} \wedge r \leq h \\ 2(h-r)^3 r^3 - \frac{h^6}{64} & r > 0 \wedge r \leq \frac{h}{2} \\ 0 & \text{Otherwise} \end{cases} \quad (12)$$

where L is the size of the cell, h the smoothing length and r the distance between the particles under consideration ($X_i - X_j$). Considering the kernel proposed by Akinci et al. [25], an extra flat spot is added to nullify the forces in the particles when they are close to each other. This flat spot reduces the vibrations of the particles in the equilibriums points at higher time-steps. The flat spots is assumed to be at a $\pm 5\%$ distance between the cell size of a single fluid particle, hence allowing only 5% overlap and more smoothed stabilization. The surface tension force curve using the above kernel is illustrated in Figure 2.4. It has to be noted that the surface tension force curve attracts the fluid particle in the region of smoothing length and hence maintains a minimum surface area. The particles in the free surface will have a high energy and the surface tension coefficient γ is temperature dependent (from Table 2.1). The curvature of the deposit profile depends on the temperature and the total time the metal remains in fluid state which is dependent on the process parameters like power and scan velocity. The relationship of the input parameters and their relationships to the output is discussed in detail in the results section.

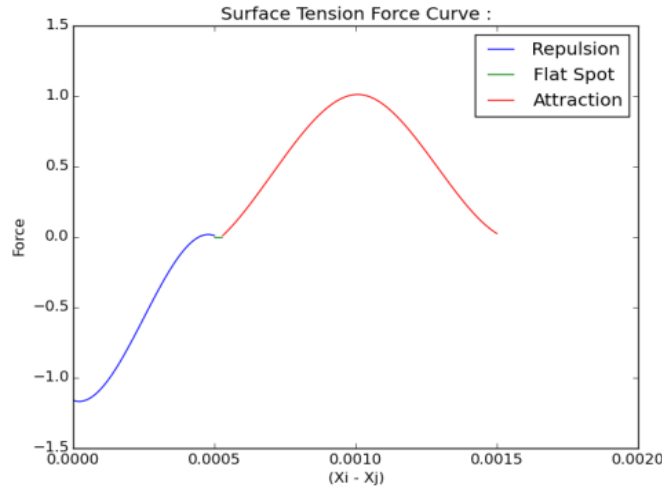


Figure 2.4: Surface tension force curve

It can be clearly realized from the curve that if the particles are within the range of the kernel, there will be a force of attraction and if the particle overlap each other there will be a force of repulsion at close distances. In the current model, the same force curve is used to model solid to fluid interaction with a higher scaling factor which gives strong adhesion and wetting with a much higher force.

2.3.2 Viscosity. There has been significant efforts to determine a more realistic viscous force using particle based dynamics [22] [26]. Since the surface tension force have very narrow smoothing regions and the magnitude is much lesser compared to the gravity force, the viscous force plays an important role in stabilizing the velocities. The viscosity force curve function implemented in the current work can be written as:

$$F_{i \leftarrow j}^{viscosity} = \mu \sum_j m_j \frac{v_j - v_i}{\rho_j} \nabla^2 W(|X_i - X_j|, h) \quad (13)$$

where μ is the dynamic viscosity coefficient obtained from Table 2.1, m the mass of the particle, v the velocity of the particle, X the positions of the particle and the kernel $\nabla^2 W$ is given by:

$$\nabla^2 W(|X_i - X_j|, h) = \frac{45}{\pi h^6} (h - |X_i - X_j|) \quad (14)$$

It is to be noted that, the coefficient of dynamic viscosity μ is temperature dependent (from Table 2.1). Hence the force due to viscosity is highly dependent on temperature of the interacting particle, which illustrates a more realistic molten metal viscous flow. Viscosity force curve with variable dynamic viscosity coefficient μ is illustrated in Figure 2.5.

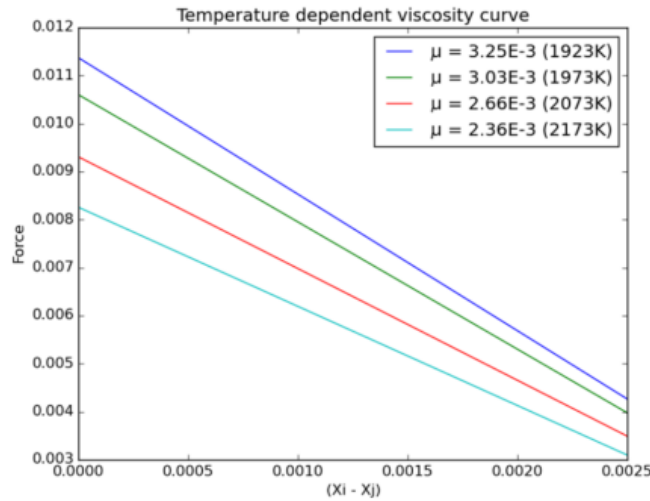


Figure 2.5: Viscosity force curve

2.3.3 Thermal Expansion. Thermal expansion is an important factor that needs to be considered in modeling heat problems which takes into account fluid motion. The temperature rise in the fluids increase the kinetic energy of the particles which begin moving more and maintain a greater separation. The complex phenomenon of thermal expansion is not considered in the current work. However a simpler model is proposed to take into account the effects of thermal expansion by modifying the surface tension curve as the fluid temperature increases. The linear increase in the size of the fluid particle due to thermal expansion can be written as:

$$\Delta L = \alpha_L L \Delta T \quad (15)$$

where ΔL is the change in cell size due to thermal expansion, α_L is the linear thermal expansion coefficient (from Table 2.1), L the original size of the cell and ΔT the temperature

change of the particle under consideration. The change in the surface tension force curve taking thermal expansion into account is illustrated in the Figure 2.6.

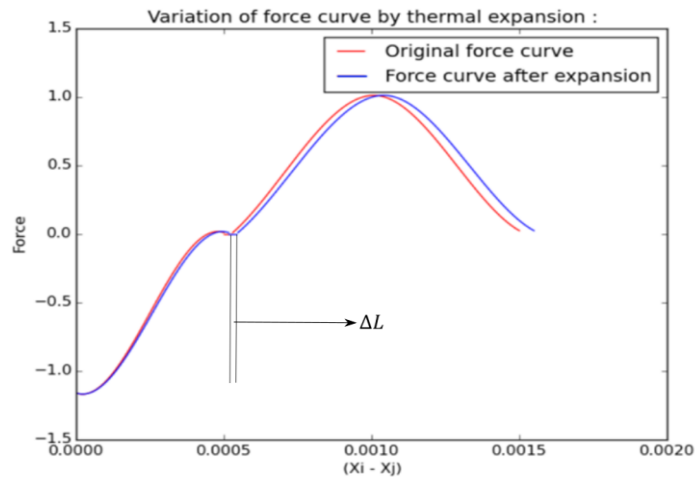


Figure 2.6: Force curve variation under thermal expansion

The fluid particles are applied with the above discussed forces, and gravitational force from which dynamic velocities are calculated in each time step. An adaptive time stepping algorithm ensures the fluids from overlapping beyond the required limit and hence maintains the stability of the model.

3 EXPERIMENTAL SETUP

3.1 Material

The material used in conducting experiments in the current study is grade 23 Ti-6Al-4V ELI alloy. The substrates are 2×0.5×0.25 inches (50.8×12.7×6.35 mm) rectangular bars and the wire is 0.0630 inch (1.6mm) diameter. Ti-64 ELI is a higher-purity ("extra-low interstitial") version of Ti-64, with lower specified limits on iron and the interstitial elements C and O. It is an alpha + beta alloy which has good weld ability, highly resistant to general corrosion in most aqueous solutions, as well as in oxidizing acids, chlorides (in the presence of water), and alkalis. The chemical composition of grade 23 Ti-64 ELI alloy is outlined in the Table 3.1.

Table 3.1 : Chemical composition of grade 23 Ti-6Al-4V ELI alloy

Element	Ti	Al	V	Fe	C	N	H
Content %	88.09 - 91	55.5 – 6.5	3.5 – 4.5	≤ 0.25	≤ 0.080	≤ 0.030	≤ 0.012

3.2 Design of Experiments (DOE)

The experiments conducted for the current study were primarily divided into two identical sets. Set one consists of experiments in which the laser is scanned over the substrate. This set was conducted to study the effect of laser power and scan speed to width, depth, and stabilization distance of the dilution zone. The second set of experiments were conducted with the same factors with deposition. This study gives clear information about the deposit profile (width and height) and contact angle.

A central composite design (CCD) is used to determine the experimental runs for the current work. The CCD methodology is highly useful in determining the response behavior without performing complicated three level experiments with more replications. CCD methodology takes into consideration the variation between the points and linear regression can be used to iteratively obtain more responses. The factors used in the experiments are power (P) and power density (P_d) given by the equation:

$$P_d = \frac{P}{V_s \times D_s} \quad (16)$$

where P is the laser power, V_s the laser scan speed and D_s the laser spot diameter. The laser spot diameter is measured to be 3 mm and maintained constant throughout the experiments. The design contains an embedded factorial or fractional factorial design with center points that is augmented with a group of 'star points' that allow estimation of curvature which is given by the variable α . The precise value of α depends on the number of factors involved given by the equation.

$$\alpha = [2^k]^{\frac{1}{4}} \quad (17)$$

In this case the k value is 2 and hence value of α is given by 1.414. The star points are calculated based on α values. The experiments performed in this work is a central composite circumscribed (CCC) methodology which considers the data points outside the range of specified values as shown in Figure 3.1 and the data points are listed in Table 3.2. The same factors and levels are used for both the experimental sets, i.e. scanning and deposition.

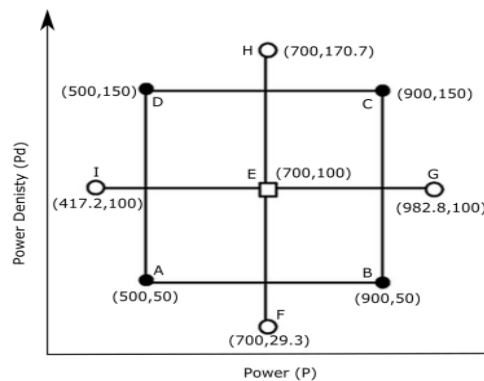


Figure 3.1: Central composite design with data points

Table 3.2: Data points obtained by DOE

Point	Power (P) W	Power density (P_d) $Wmm^{-2}s$
A	500	50
B	900	50
C	900	150
D	500	150
E	700	100
F	700	29.3
G	982.8	100
H	700	170.7
I	417.2	100

3.3. Experimental Setup

The laser scanning experimental setup consists of a fixture as shown in the Figure 3.2 which holds the substrate flat and also gives close agreement to the boundary conditions applied in the model exposing the top, sides and bottom surfaces.

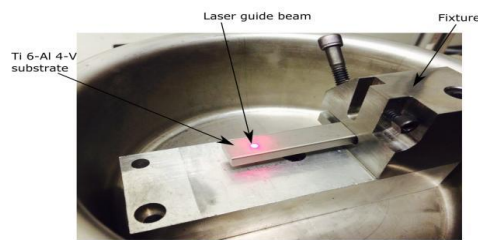


Figure 3.2: Laser scanning experimental setup

The wire deposition experimental setup shown in Figure 3.3, has the same arrangement with a wire holding mechanism which holds the wire flat on the substrate. The travel direction illustrated in the Figure 3.3 is consistent throughout the experimental runs.

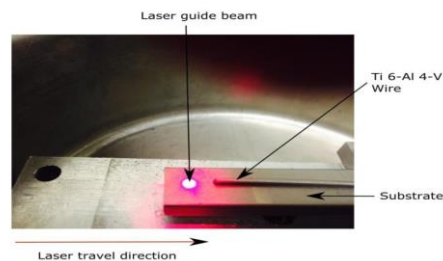


Figure 3.3: Laser deposition experimental setup

The laser used in all the experimental runs is a single mode CW Gaussian beam fiber laser. As mentioned earlier the spot size is measured with the help of guide beam by adjusting the focal length and maintained constant at 3mm. The travel length of the laser is constant at 30 mm from the starting point in the direction of travel. The experiment chamber is maintained inert with compressed argon gas to prevent oxidation. The complete experimental setup is revealed in Figure 3.4.

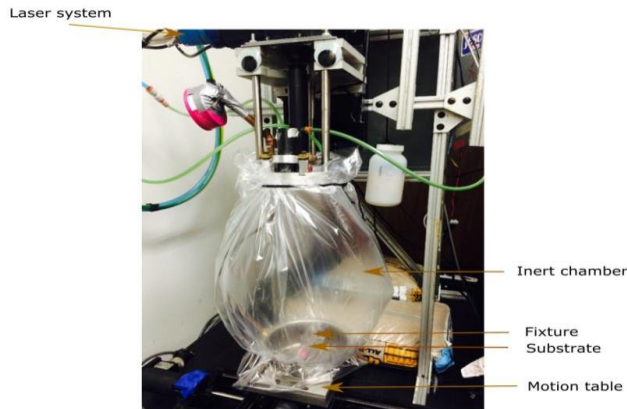


Figure 3.4: Experimental setup

3.4 Sample Preparation

The experiments were conducted based on the data points obtained from DOE and a completely randomized experimental runs were followed for the scanning and deposition. The scanned substrates were used to measure the scan width, and stabilization distance. The laser scanned substrate is shown in Figure 3.5. The deposited substrates are used to obtain the deposit height and width. The deposited substrate is shown in Figure 3.6.



Figure 3.5: Laser scanned substrate



Figure 3.6: Laser deposited substrate

The scanned and deposited substrates after completion of the measurements were cross sectioned with the help of a wire Electrical Discharge Machine (EDM). The cross sections were made at 2 predefined points which is consistent for all the samples. The samples were mounted in Bakelite, ground and polished to 0.5 micron surface finish. The polished samples were etched using Kroll's Reagent (mixture of distilled water, nitric acid and hydrofluoric acid) to distinguish the dilution zone and heat affected zone to measure the melt pool depth from the scanned samples. The cross sections of deposited substrates are used to measure the deposit height and contact angle of the profile.

4 PARAMETER DETERMINATION

The material properties taken into consideration in the model have clear agreement with the properties of Ti-64 alloy [14] [15] [16]. However the particle based approach is generally utilized in computer graphics and animation due to its high ability to numerically solve real time fluid and gas problems. There are many kernels that have been developed to solve the fluid forces like surface tension and viscosity [17] [18] [19]. However the accuracy of the smoothing kernels has been found to be varying for different applications. Generally the kernels have to be fine-tuned to determine its scale or the amplification factor to achieve a close agreement. The scaling factors of the curves are highly dependent on the resolution of the model (number of particles) and time step utilized. Many previous attempts in SPH fluid modeling have predetermined number of particles which assists the developers to select a suitable scale and kernel for the application under study. The current model on the other hand has a dynamic solid to fluid exchange on melting and fluid to solid exchange on solidification. This dynamic behavior limits the efficient determination of the scaling factor of the kernel since it is highly dependent on the input factors.

To achieve a close agreement of the fluid model and the experiment, a physical experimental results based approach has been followed. This section briefly explains the parameters determination of the model from experimental data. Since the heat model is proven to have close agreement to the process from many previous attempts in the modeling of additive manufacturing, the fluid model have been given primary emphasis. Two physical measurements, deposit height and width are taken into consideration for this calculation. The reason being, these two measurements are highly dependent on every assumptions and calculations in the model, i.e. heat model determines the heat flow and temperature rise, which determines the number of fluid particles. It is also highly dependent on the variation in the factors of the experiment i.e. power and scan speed. The time for which the molten metal remains as fluid depends on the scan speed and power, which controls the spread of the fluid by viscosity and curvature by surface tension. An example of physical experimental data with 900 W power, 2 mm/s scan speed (power density 150) illustrating deposit height and width is shown in Figure 4.1 is taken into consideration for comparison.

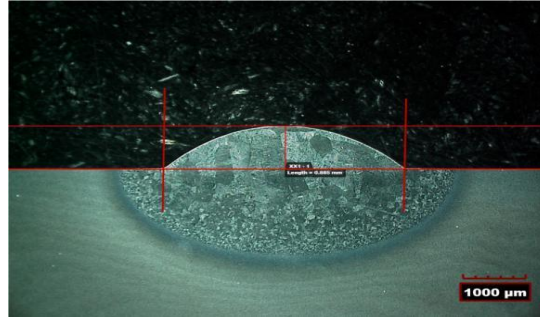


Figure 4.1: Image from optical microscope illustrating deposit height and width measurement for 900 W and 2 mm/s scan speed

The parameters under consideration are the scaling factors of the surface tension curve for cohesion and adhesion illustrated in Figures 2.4. The third factor is the scaling factor of the viscosity force curve illustrated in figure 2.5. A factorial design of experiments were followed in the model to determine these values which have close agreement to the physical data. 3^3 Factorial experiment was performed in the model by varying the values of these factors. The results from each of the 27 model runs was compared with the experimental data to evaluate the point at which minimum variation is achieved using the equation:

$$\text{Variation} = |Width_{\text{experiment}} - Width_{\text{model}}| + |Depth_{\text{experiment}} - Depth_{\text{model}}| \quad (18)$$

The next step in the procedure is to keep the point at which there is minimum variation as the center point and perform serial factorial experiments until the variations are minimum around one point. This procedure is repeated for other data points to finalize the optimum process parameters of the forces which are utilized in the model for experimental validation. It has been found that all the data points gave minimum variation at same range of values which was implemented in the model. This model is validated at a data point which was not used to perform the DOE and was compared with the physical experiments. The results were highly promising and gave a clear range of the values of unknown factors. This attempt provides a close agreement of the model and the experimental results which accounts for all possible errors occurring from force curve assumptions.

5 RESULTS

5.1 Numerical Model Results

A numerical model of wire deposition was performed to study the thermal and fluid behavior during wire feed. The substrate used is Ti-6Al-4V, 50.8×12.7×6.35 mm rectangular block and wire used is 1.6 mm diameter. The laser power is 700 Watts with the spot size of 3 mm. The laser scan speed is 5 mm/s and wire feed rate is 10 mm/s. Both the laser and wire feed system are assumed to be attached to the same apparatus, hence the velocity of wire feed into the

weld pool is highly depended on the resultant velocity. This assumption is made to closely match with a laser aided wire deposition system. The angle of wire feed is assumed to be 30 degrees in the X-Z axis with respect to the horizontal. The time based results obtained from the model is plotted using POV-Ray 3D rendering tool and revealed in Figure 5.1.

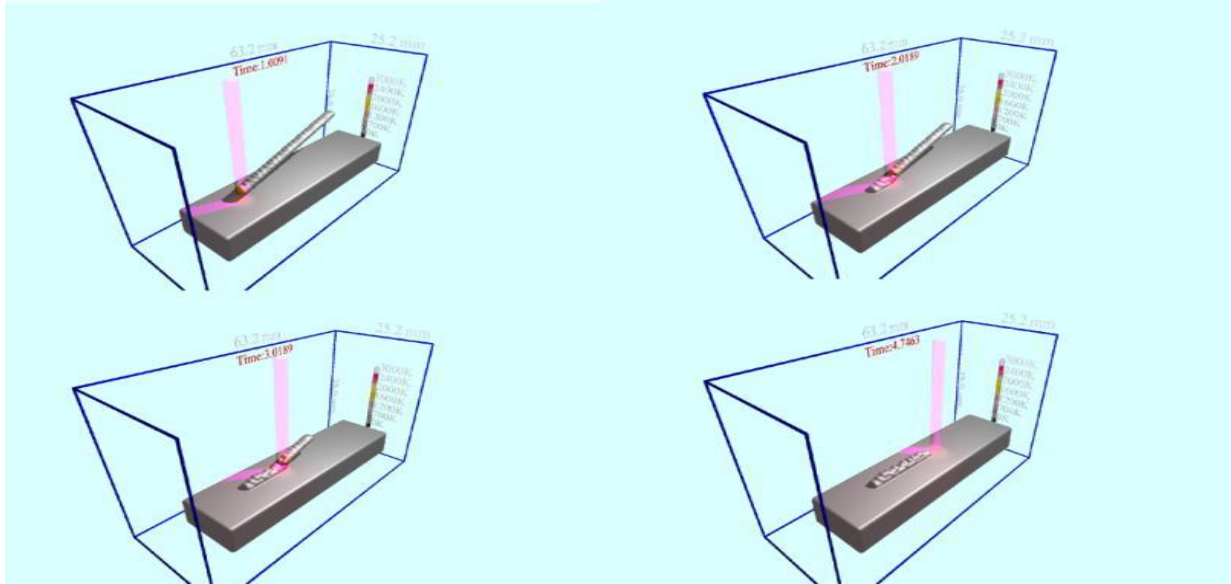


Figure 5.1: Wire deposition results at time 1.0091s, 2.0189s, 3.0189s and 4.7463s

As discussed earlier, the primary focus of this study was to establish a relationship between model with the experiments for its heat and fluid characteristics with and without material deposition. Hence the deposition experiments was conducted by placing the wire straight and flat on the substrate and scanning laser in a straight line for deposition. This set up will give a more detailed effect of the material parameters on the model and its agreement with the experimental results without being affected by the wire parameters like wire feed rates, feed directions and feed angle. The initial setup of the model for scanning and wire deposition model is shown in Figure 5.2.

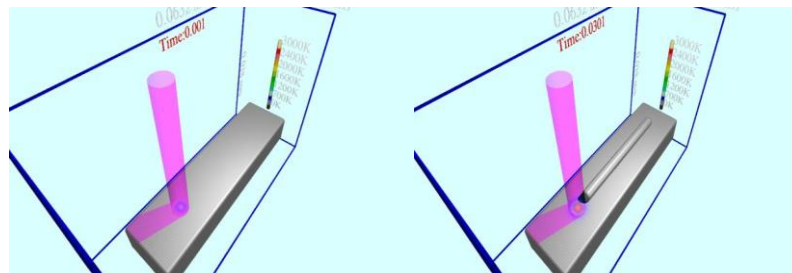


Figure 5.2: Initial setup of the model for scanning and deposition

The top view of time based temperature results obtained from the scanning model in a total simulation time of 12.2136 seconds for 700 Watts and power density $100 \text{ Wmm}^{-2}\text{s}$ (laser scan speed 2mm/s) is revealed in Figure 5.3. Similarly the results of wire deposition from the model is obtained for the same conditions are illustrated in Figure 5.4.

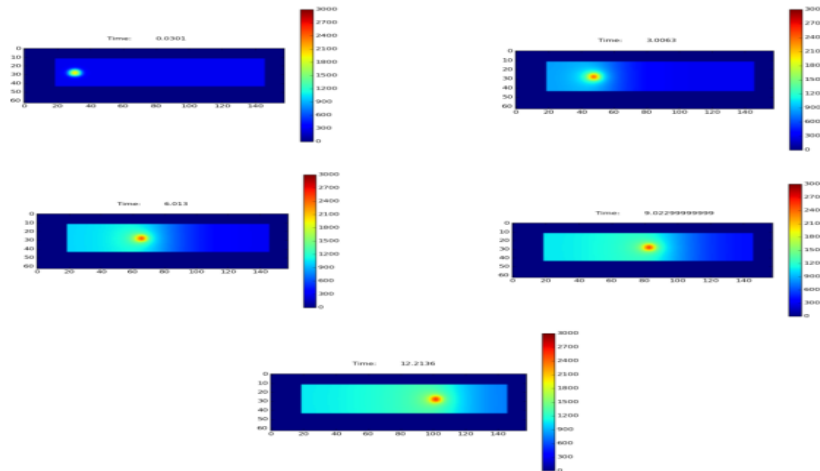


Figure 5.3: Temperature results of laser scanning with power 700W and laser speed 2 mm/s

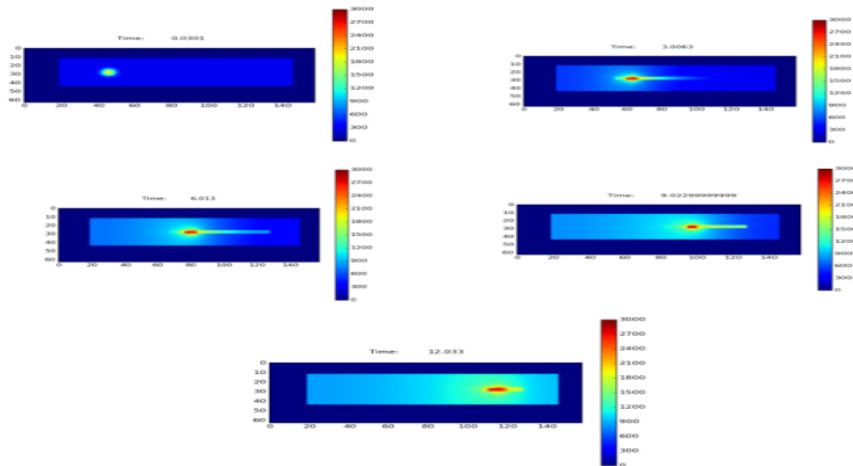


Figure 5.4: Temperature results of wire deposition with power 700W and laser speed 2 mm/s

5.2 Experimental Results and Validation

Experiments were conducted based on the data points obtained from DOE as shown in Table 3.2. The 9 experimental runs are conducted with 2 replications for scanning and deposition which provided the data from 36 samples. All the experimental runs were simulated from the model with the exact initial conditions and parameters for comparison of the results.

5.2.1 Scan Width. The width of the laser scan obtained from the experiment and model were compared to establish their agreement. The scanned substrates were observed under the optical microscope and width measurements are taken. The width measurements are recorded from the middle of the scan to avoid stabilization errors during the start and the end of the scan. The comparison of scan width from one of the data points of the experiment and model is illustrated in Figure 5.5. The comparison of all the data points for scan width between experiment and model is shown in Figure 5.6.



Figure 5.5: Comparison of scan width of experiment and model for laser power 500 W and scan speed 3.33 mm/s

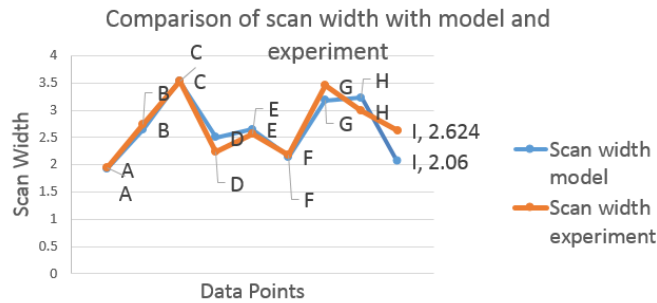


Figure 5.6: Comparison of the scan width of experiment and model for different data points by varying laser power and scan velocity

5.2.2 Stabilization Distance. Stabilization distance is the distance from the starting point of the laser scan to the point along the line of scan at which the scan width remains stable. This parameter gives a good agreement of the variation of the width of melt pool width with respect to the power and scan speed. Validation of the stabilization distance establishes the accuracy of the heat model used in this study. The stabilization distance of the experiment and model are illustrated in the Figure 5.7 and Figure 5.8 shows the comparison for different data points between experiment and model.

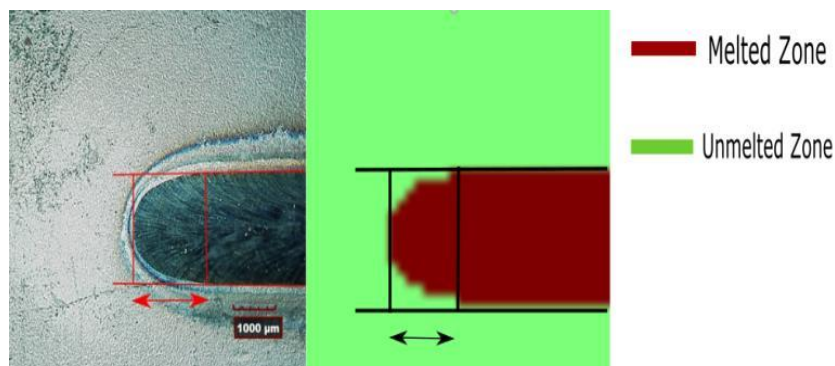


Figure 5.7: Stabilization distance comparison of experiment and model at 700 W power and 7.96 mm/s scan speed

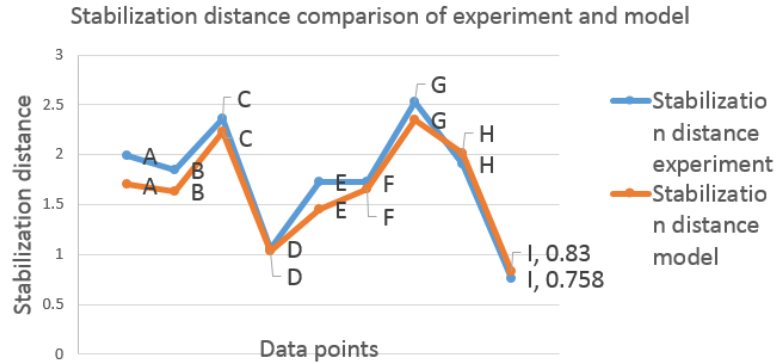


Figure 5.8: Comparison of the stabilization distance of experiment and model for different data points by varying laser power and scan velocity

5.2.3 Melt Pool Depth. The cross sectioned samples from the laser scanned substrates when etched with Kroll's reagent clearly distinguishes the solidified melt pool and heat affected zones. The depth of this zone from the free surface of the substrate is measured and compared with the model as revealed in Figure 5.9. This establishes a close agreement of the Gaussian laser beam and heat transfer effects with the model and experiment. The comparison of the melt pool depth for the data points are illustrated in the Figure 5.10.

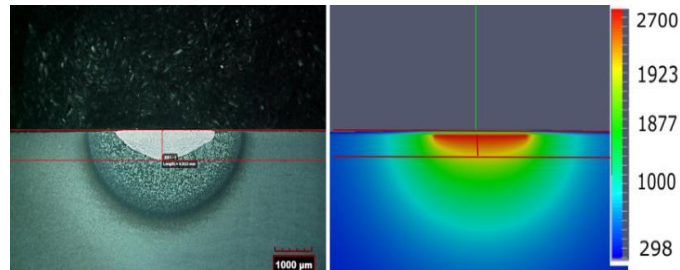


Figure 5.9: Melt pool depth comparison of experiment and model at 700 W power and 2.33 mm/s scan speed

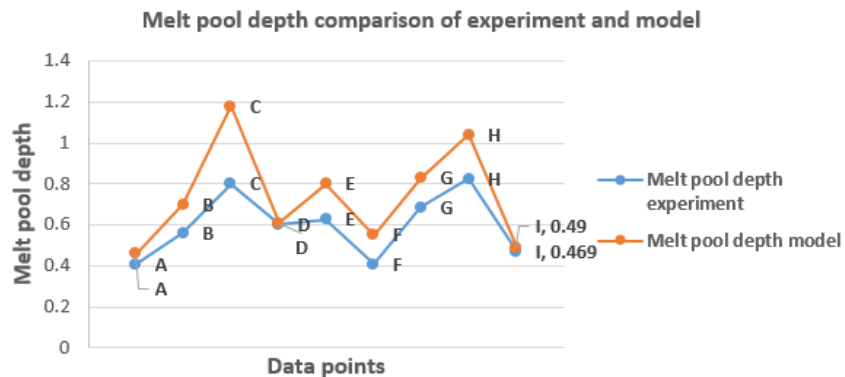


Figure 5.10: Comparison of the melt pool depth of experiment and model for different data points by varying laser power and scan velocity

5.2.4 Deposit Height. The deposited substrates are analyzed for obtaining the height of the single layer deposit from the experiment. The deposit height varies with the laser power and scan speed. The comparison establishes a good relationship between the fluid model and the experimental results. The height of the deposit is a critical parameter that establishes close agreement of the surface tension, viscosity and thermal expansion of the model with the experimental results. A laser displacement sensor is used to measure the height of the deposits from the samples. The 3D height measurement feature of the optical microscope is also used to obtain the deposit height is illustrated in Figure 5.11.

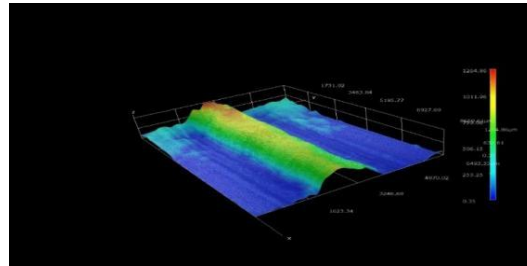


Figure 5.11: 3D image from optical microscope illustrating the heights of the deposit at different regions

The 3D profile is sliced at specific points where the cross sections were made using the EDM. Cross sectional images from the optical microscope were used to obtain the deposit profile and height as depicted in Figure 5.12. Comparison of deposit height of all data points from the experiment and model is revealed in Figure 5.13.

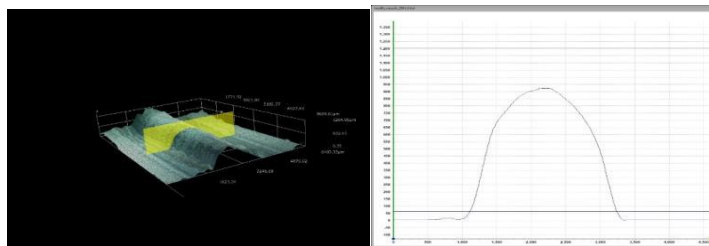


Figure 5.12: Cross sectional image of deposited substrate using optical microscope

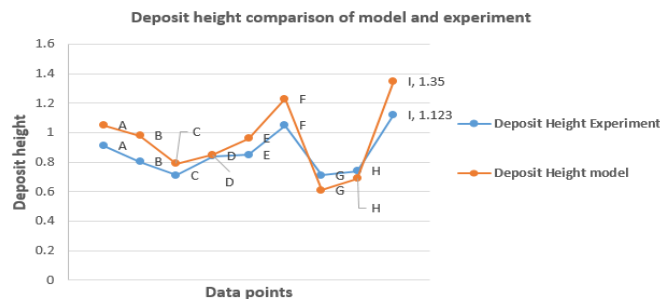


Figure 5.13: Comparison of the deposit height from experiment and model for different data points by varying laser power and scan velocity

5.2.5 Deposit Width. The width of the deposit is highly affected by the fluid characteristics especially thermal expansion. The shift in the surface tension force will exert more outward force to the fluids resulting in the spread of fluid to a higher width. These fluid properties vary with the factors since the time of laser power and power density varies the time for which the metal is in fluid form before solidification. The comparison of the deposit height between experiment and model is shown in Figure 5.14 and the comparison of all the experimental runs is shown in Figure 5.15.

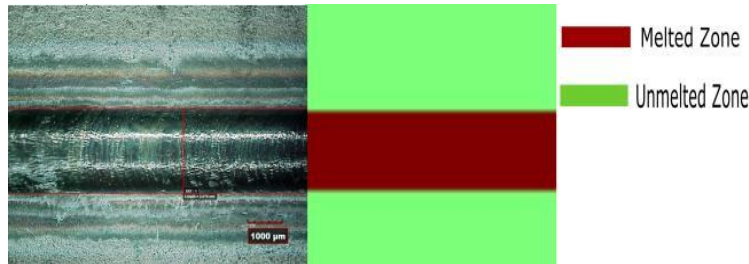


Figure 5.14: Deposit width comparison of experiment and model at 500 W power and 3.33 mm/s scan speed

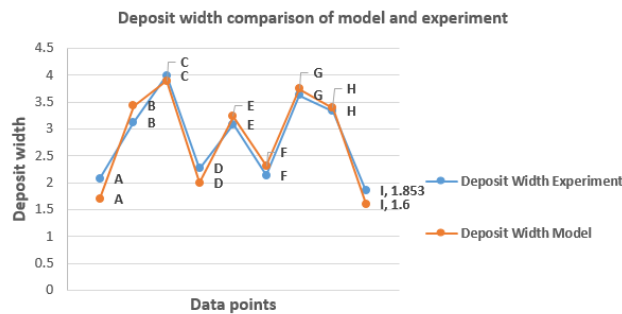


Figure 5.15: Comparison of the deposit width from experiment and model for different data points by varying laser power and scan velocity

5.2.6 Contact Angle. The contact angle is the angle, measured through the liquid, where a liquid interface meets a solid surface. Contact angle is also known as “wetting angle”, which quantifies the wettability of a solid surface by a liquid. The cross section of the deposited substrates clearly reveals the contact angle of the molten fluid at the instance of solidification. Contact angle comparison of one data point from experiment and model is shown in Figure 5.16. Comparison of all data points are illustrated in Figure 5.17.

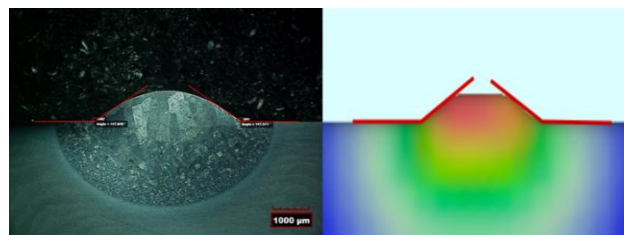


Figure 5.16: Contact angle comparison of experiment and model at 900 W power and 2 mm/s scan speed

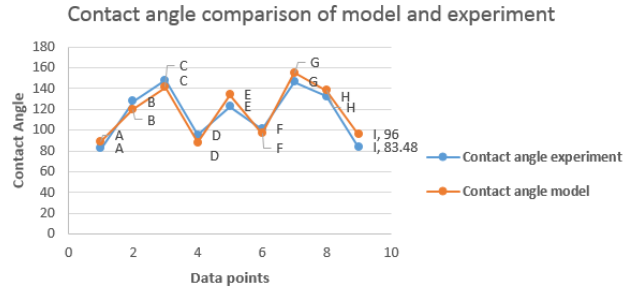


Figure 5.17: Comparison of the contact angle from experiment and model for different data points by varying laser power and scan velocity

6 CONCLUSION

A numerical 3 dimensional model of wire feed additive manufacturing realizing the effect of heat and fluid flow was developed. The model considers a ray traced Gaussian laser beam which takes into account the effects of general modes of heat transfer i.e. conduction, convection and radiation. The fluid model was developed by implementing approaches from smoothed particle hydrodynamics (SPH). A central composite design of experiments was performed to determine 9 levels of the factors, power and power density. The experiments were conducted with scanning and wire deposition with the wire stationary on the substrate to avoid wire feed parameters which are not considered in this study.

The scanned and deposited substrates are analyzed to measure scan width, stabilization distance, scan depth, deposit height, deposit width and contact angle for validation. The scope of the model is limited to macroscopic properties like deposit and scan profile. However microscopic characteristics like microstructure evolution and grain growth cannot be determined by the current implementation of the model. This requires a different algorithm and a higher resolution approach. The unknown parameter determination step provided a good agreement of the model and experiments for the above mentioned parameters. It can be concluded that the model can efficiently predict the wire feed deposition characteristics based on material properties and can also be used for other materials.

Acknowledgements

The authors would like to express their sincere gratitude to the support from National Aeronautics and Space Administration (Grant Number NNX11AI73A) and Laser Aided Manufacturing Laboratory at Missouri University of Science and Technology.

References

- [1] Dongbong Ding, Zenxi Pan, Dominic Cuiuri, Huijun Li (2015). “Wire-feed additive manufacturing of metal components: technologies, developments and future interests,” International Journal of Advanced Manufacturing Technology, DOI 10.1007/s00170-015-7077-3.

- [2] Richard Martukanitz, Pan Michaleris, Todd Palmer, Tarasankar DebRoy, Zi-Kui Liu, Richard Otis, Tae Wook Heo, Long-Qing Chen, (2014). "Toward an integrated computational system for describing the additive manufacturing process for metallic materials," *Science Direct Additive Manufacturing* 1-4 (2014)-52-63.
- [3] Qun Tang, Shengyong Pang, Binbin Chen, Hongbo Suo, Jianxin Zhou (15 July, 2014). "A three dimensional transient model of heat transfer and fluid flow of weld pool during electron beam freeform fabrication of Ti-6-Al-4-V alloy," *International Journal of heat and Mass transfer*.
- [4] Zhiqiang Fan and Frank Liou (16 March 2012). "Numerical Modeling of Additive Manufacturing (AM) of Titanium Alloy," *Intech* DOI: 10.5772/34848.
- [5] T.A. Krol, C. Seidel, J. Schilp, M. Hofmann, W. Gan, M.F. Zaeh (2013). "Verification of structural simulation results of metal-based additive manufacturing by means of neutron diffraction," *Science Direct, lasers in manufacturing conference*, 2013.
- [6] Pulin Nie, O.A. Ojo, Zhuguo Li (2014). "Numerical modeling of microstructure evolution during laser additive manufacturing of a nickel-based super alloy," *Science Direct, Acta Materialia* 77 (2014) 85-95.
- [7] J.C. Heigel, P. Michaleris, E.W. Reutzel (2014). "Thermo-mechanical model development and validation of directed deposition additive manufacturing of Ti-6Al-4V," *Science Direct, Additive Manufacturing* 5 (2015) 9-19.
- [8] Panagiotis Michaleris (2014). "Modeling metal deposition in heat transfer analysis of additive manufacturing process," *Elsevier Finite Elements in Analysis and Design* 86 (2014) 51-60.
- [9] Jason Fox and Jack Beuth. "Process mapping of transient melt pool response in wire feed additive manufacturing of Ti-6Al-4V," *SFF Symposium*.
- [10] Ninggang Shen and Kevin Chou (2012). "Numerical thermal analysis in electron beam additive manufacturing with preheating effects," *SFF Symposium* 2012.
- [11] Shengyong Pang, Xin Chen, Jianxin Zhou, Xinyu Shao and Chunming Wang (2015). "3D transient multiphase model for keyhole, vapor plume, and weld pool dynamics in laser welding including the ambient pressure effect," *Elsevier Optics and Lasers in Engineering*.
- [12] Shengyong Pang, Weidong Chen, Jianxin Zhou and Dunming Liao (2014). "Self-consistent modeling of keyhole and weld pool dynamics in tandem dual beam laser welding of aluminum alloy," *Elsevier Journal of Materials processing Technology*.
- [13] G. Casalino, N. Contuzzi, F. M. C. Minutolo and M. Mortello. "Finite element model for laser welding of titanium," *CIRP ICME' 14*.
- [14] Alessandro Franco, Luca Romoli, and Alessandro Musacchio (2014). "Modelling for predicting seam geometry in laser beam welding of stainless steel," *International Journal of Thermal Sciences*.
- [15] Holoor. "Optical vortex plate application notes," http://www.holoor.co.il/Diffractive_optics_Applications/Application%20notes/Optical%20vortex%20phase%20plate%20application%20notes.pdf
- [16] Rusty Rook, Mehmet Yildiz and Sadik Dost, "Modeling transient heat transfer using SPH and implicit time integration," *Numerical heat transfer, Part B: Fundamentals: An International of Computation and Methodology*.

- [17] Paul W. Cleary, “Modelling confined multi-material heat and mass flows using SPH,” International conference on CFD in Mineral & Metal Processing and Power Generation CSIRO 1997.
- [18] John H. Leinhard IV and John H. Leinhard V “A heat transfer textbook,” Third edition.
- [19] Mills, K.C. (2002). “Recommended Values of Thermophysical Properties for Selected Commercial Alloys,” Woodhead Publishing Ltd, ISBN 978-1855735699, Cambridge.
- [20] Boyer. R., Welsch. G, Collings. E.W (1994). “Material properties handbook: titanium alloys, ASM International, ISBN 978-0871704818, Materials Park, OH.
- [21] Lips, T. & Fritsche, B. (2005). A comparison of commonly used re-entry analysis tools, Acta astronautica, Vol. 57, No. 2-8, (July-October 2005), pp.312-323, ISSN 0094-5765.
- [22] Markus Becker and Matthias Teschner (2007). “Weakly compressible SPH for free surface flows,” Eurographics/ACM SIGGRAPH Symposium on Computer Animation (2007), pp. 1-8.
- [23] Nui Galway. “Mesh-free computational fluid dynamics,” <http://www.nuigalway.ie/engineering-informatics/biomedical-engineering/research/mesh-freecomputationalfluidynamics>.
- [24] “Smoothed Particle Hydrodynamics,” <http://www.aer.mw.tum.de/en/research-groups/komplexe-fluide/smoothed-particle-hydrodynamics>.
- [25] Nadir Akinci, Gizem Akinci and Matthias Teschner. “Versatile surface tension and adhesion for SPH fluids,” ACM Transactions on Graphics (TOG) - Proceedings of ACM SIGGRAPH Asia 2013 Volume 32 Issue 6, November 2013 Article No. 182.
- [26] Jacek Pozorski and Arkadiusz Wawrenczuk (2002). “SPH computation of incompressible viscous flows,” Journal of theoretical and applied mechanics 40, 4, pp. 917-937.